PERGAMON

Engineering Fracture Mechanics 69 (2002) 1977–1996

Engineering Fracture Mechanics

www.elsevier.com/locate/engfracmech

Experimental and mathematical modeling for fracture of rock joint with regular asperities

T.H. Huang [a], C.S. Chang [b,*], C.Y. Chao [c]

[a] *National Taiwan University, Taipei, Taiwan 106, ROC*

[b] *Department of Civil and Environmental Engineering, University of Massachusetts, 253 Marston Hall, Box 35205, Amherst, MA 01003-5205, USA*

[c] *Chung-Cheng Institute of Technology, Tauyen, Taiwan 320, ROC*

Received 22 March 2002; accepted 16 April 2002

Abstract

This paper is aimed at developing a mathematical model for the deformation behavior of a rock joint that explicitly accounts for the effects of joint surface topography. The present work is focused on rock joints with triangle-shaped regular asperities. Specimens of artificial rock joint with triangle-shaped asperities were made of simulated rock material and tested in the laboratory. Experimental results are examined to identify three mechanisms that influence the deformation of a rock joint: sliding, separation of asperity contact-faces, and shear fracture of asperities. A modeling methodology is then described and the behaviors of an asperity contact-face, including separation, sliding and shear fracture are discussed. The stress–deformation relationship of a rock joint is subsequently derived and the model performance is evaluated by comparing the predicted results from the derived model and the measured results from experiments.

Keywords: Fracture; Rock joint; Shear behavior; Dilation; Friction

1. Introduction

The mechanical behavior of rock joints is complex and influenced by a great variety of factors, such as rock elastic properties, mineral friction, surface adhesion, surface roughness (i.e. topography), and presence of fluids and debris at the interface. In this paper, we focus on the influence of surface roughness of a rock joint on its mechanical behavior. A number of empirical equations have been developed to correlate the roughness coefficient to the shear strength of a rock joint (e.g., [1–3]). However, it is desirable to model the joint behavior directly from mechanics point of view considering the effects of surface topography. Along this line, one of the earlier attempts is by Greenwood and Williamson [4], who derived a model for the interface behavior between a rough surface and a rigid smooth plane, considering the elastic deformation of

* Corresponding author. Tel.: +1-413-545-5401; fax: +1-413-545-4525.
E-mail address: chang@ecs.umass.edu (C.S. Chang).

0013-7944/02/$ - see front matter
PII: S0013-7944(02)00072-3

asperity contact-faces. The concept was later extended to study the interface behavior of two rough surfaces under normal loads (see [5–8], among others). Further, the shear behavior of an interface of two rough surfaces was studied considering only the elastic deformation of asperity contacts [9–11]. More recent studies have considered the sliding at asperity contact with the aim of obtaining shear strength of contacting rough surfaces [12–15]. Yoshioka [16] provides a review of some of the recent micromechanical methods.

For all abovementioned models, the plasticity of asperity contacts has been considered in the context of sliding; the fracture of asperities is not considered. However, for a brittle and highly fractured rock mass, it is often found that the fracture of asperities has significant effects on its shear strength and dilatancy behavior. The present work aims to develop a mathematical model that explicitly accounts for the influence of joint surface topography on the deformation and strength behavior of rock joints. Specifically, this investigation is focused on rock joints with a simple surface topography so that failure mechanisms and their effect on deformation and strength can be clearly identified. The simple surface topography of rock joints is useful to verify the developed methodology before it is extended to more complicated and realistic situations. For this purpose, instead of using natural rock joints, we manufactured artificial rock joint using simulated rock material with triangular shaped asperities as shown in Fig. 1. Based on the experimental results, observations are made to identify mechanisms that have important effects on the deformation behavior of a rock joint. We then derived the force–deformation relationships of a rock joint, which considers the observed mechanisms. The model performance is evaluated by comparing the model predictions and the experimental results.

2. Experiments for joint with regular asperities

In order to have a rock joint with well-defined triangular asperities, the rock joints are simulated in laboratory. The material is a mix of chalk, sand and water with the ratios 1:0.25:0.85 so that joint surface topology can be easily controlled and repeated. The mix is filled in a mold. When the specimen is hardened,

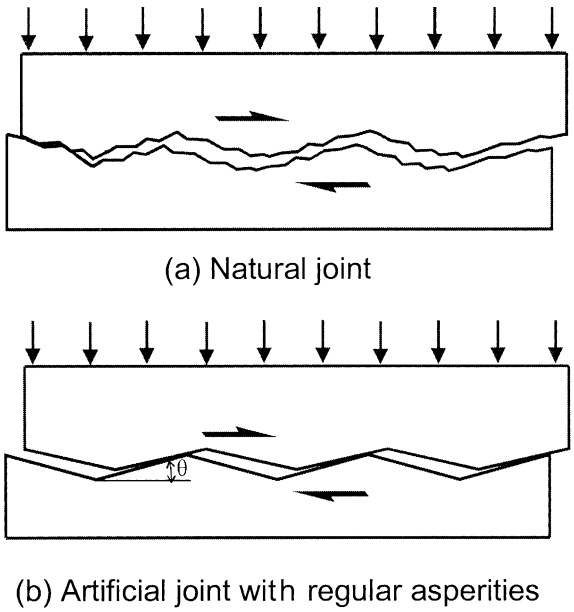

Fig. 1. Schematic plot for a specimen with regular asperities.

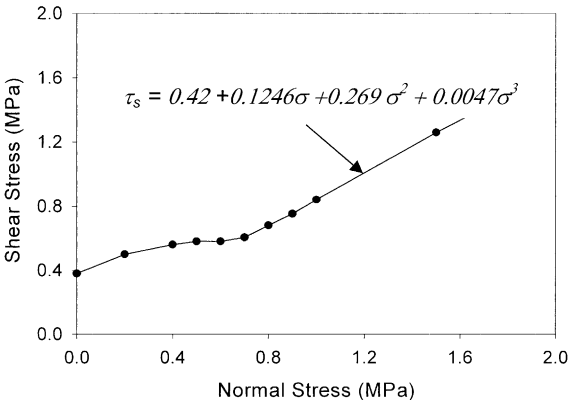

Fig. 2. Failure envelope for the simulated rock material.

it is stored in a room with temperature between 10 and 25 °C and relative humidity between 45% and 50%. The specimen is ready to use after 6–7 days when its density becomes a constant of 1.07 g/cm^3.

According to the results of uniaxial compression tests on cylindrical specimens with 54 mm in diameter and 150 mm in height, the unconfined compressive strength of the simulated material is 8.45 ± 0.16 MPa, the average Young's modulus is 6500 MPa, and the average Poisson's ratio is 0.24. The failure envelope obtained from triaxial tests is shown in Fig. 2. The ratio of compressive to tensile strength $\sigma_c/\sigma_t = 7.9$, and the ratio $E/\sigma_c = 770$. According to the classification method suggested by Deere [17], the simulated material is in the category of low strength brittle rock.

Using the simulated material, specimens of three types of interface topography have been made: (1) $\theta = 0°$ asperity (smooth interface), (2) $\theta = 15°$ asperity, and (3) $\theta = 30°$ asperity, where the base angle θ is the side inclination of the triangle-shaped asperity as shown in Fig. 1b. For each type of specimen, direct shear tests are performed under five different vertical stresses: 0.1, 0.3, 0.5, 1.0, and 1.5 MPa (see [18]).

2.1. Test results

For rock joints with 0° asperities, the shear stress–displacement curves are shown in Fig. 3. The normal compression curve is shown in Fig. 4. For rock joints with 15° asperities, the base length of each triangular tooth is 20 mm and the height is 0.258 mm. Total length of the joint specimen is 100 mm. For $\theta = 15°$ specimens, the shear stress–displacement curve are shown in Fig. 5, and the dilation curves are shown in Fig. 6. For rock joints with 30° asperities, the base length of each triangular tooth is 20 mm and the height is 0.577 mm. Total length of the specimen is 100 mm. For $\theta = 30°$ specimens, the shear stress–displacement curves and dilation curves are shown respectively in Figs. 7 and 8.

2.2. Mechanism observed

2.2.1. Failure mode

Typical failure modes observed from the specimens of the direct shear experiments are shown in Fig. 9. Four types of failure modes have been observed from these experiments, namely sliding, cut-off, separation and crushing. The occurrence of the four types of failure mode depends upon the magnitude of applied vertical stress. Under a lower vertical stress level, sliding occurs accompanied abrasion and wearing during shear friction between two surfaces. Under a higher vertical stress level, the asperities can be fractured by shear, which is termed 'cut-off' in the subsequent text. After shear fracture of the asperity, sliding takes

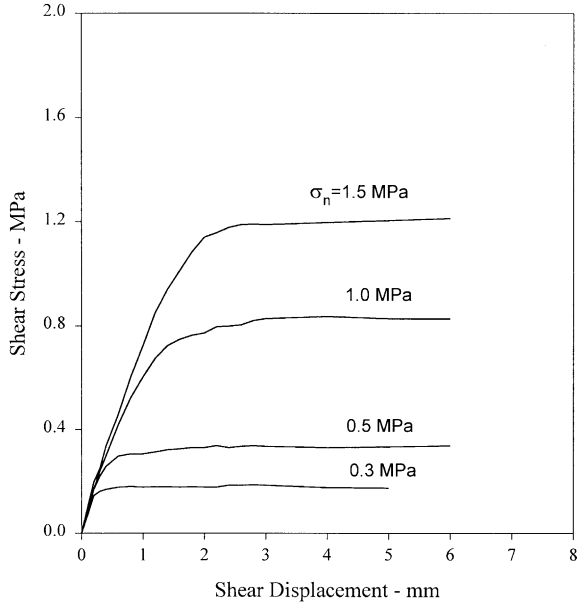

Fig. 3. Shear stress–displacement curves for joint with 0° asperities.

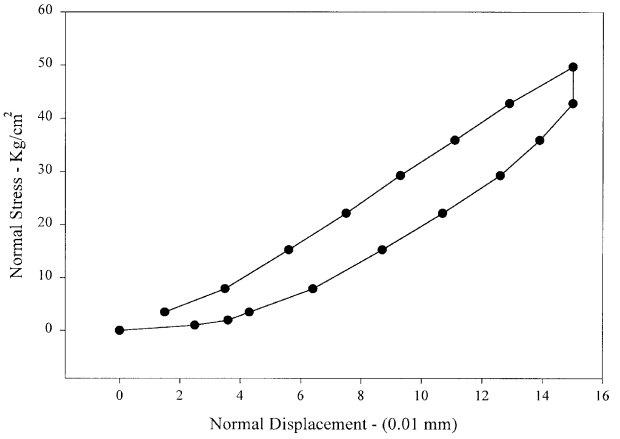

Fig. 4. Normal compression curves for joint with 0° asperities.

place on the cut-off plane. The mechanism of cut-off of asperity provides a major source for shear strength of interface [1]. As observed by Handanyan [19] and Pereira and de Freitas [20] from their experiments, asperity breakage could be caused by shear stress as well as tensile stress. Due to tight interlocking of asperities, tensile cracks may be developed at the base of asperities during shear deformation. As shown in the case of $\theta = 30°$ in Fig. 9, small tensile fractures in the direction nearly perpendicular to the surface were also observed at the base comer of the asperity. However, in our specimens, the surface topology does not provide a tight interlocking. Therefore, although mixed with small tensile fractures, the asperity breakages are primarily due to shear fractures.

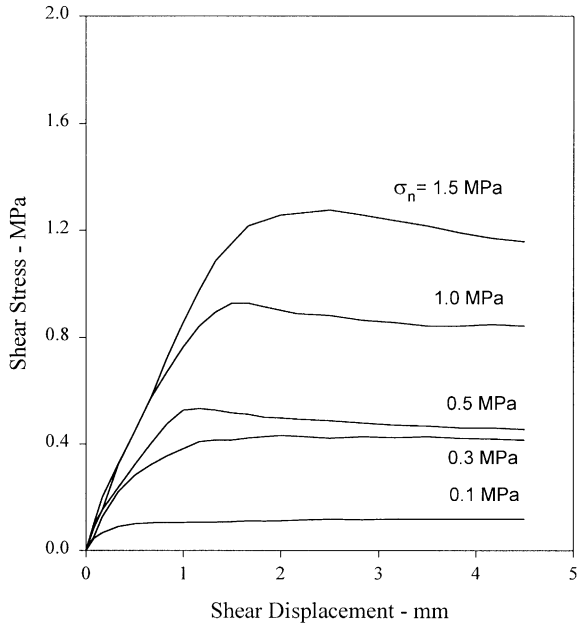

Fig. 5. Shear stress–displacement curves for joint with 15° asperities.

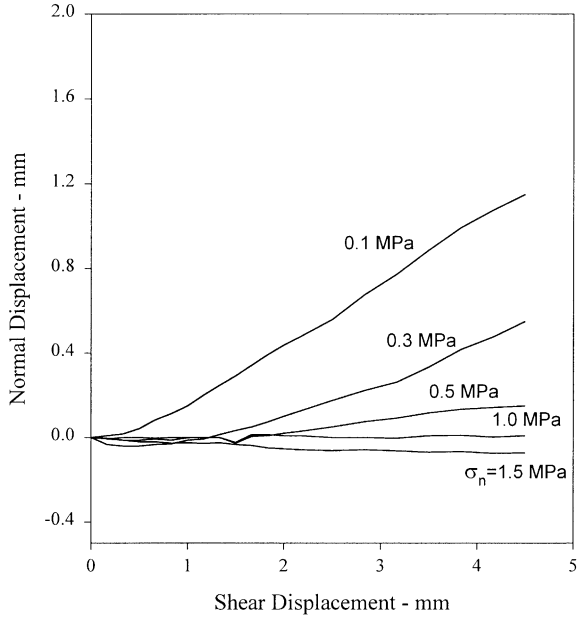

Fig. 6. Shear dilation curves for joint with 15° asperities.

For cases with low applied vertical stresses (0.1 MPa), specimens failed in frictional sliding (with abrasion and wearing). For cases with higher applied vertical stress (0.3–1.5 MPa), the asperities of

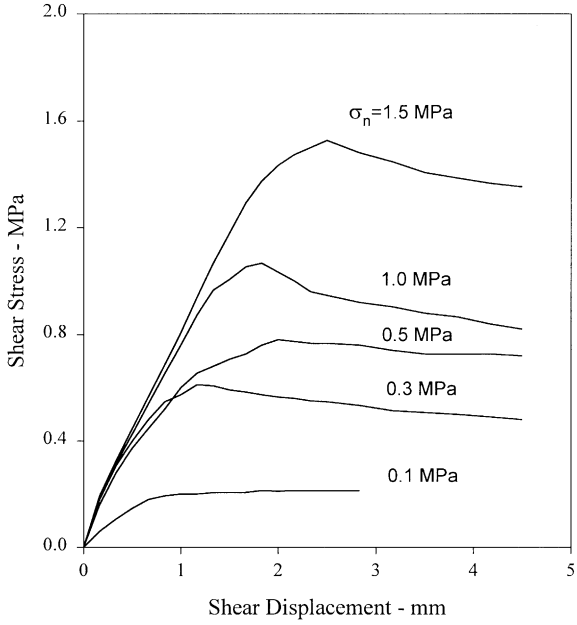

Fig. 7. Shear stress–displacement curves for joint with 30° asperities.

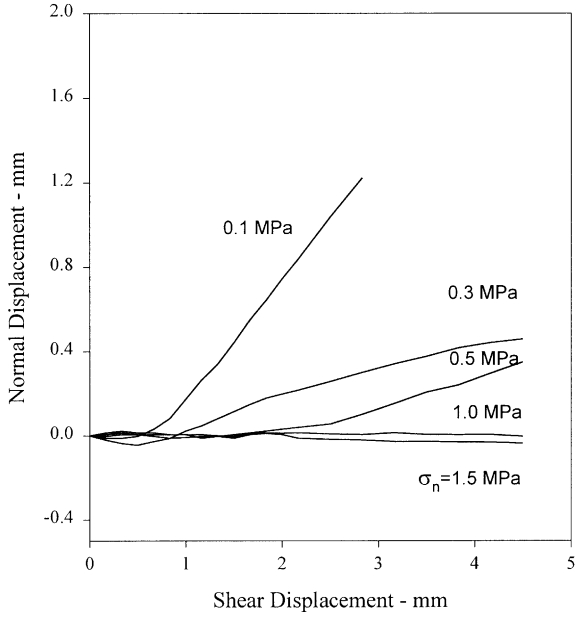

Fig. 8. Shear dilation curves for joint with 30° asperities.

specimens were cut-off. The orientation of a cut-off plane α, defined as the angle between the fractured plane and the horizontal plane, depends greatly on the magnitude of vertical stress. For $\theta = 15°$ and $\theta = 30°$,

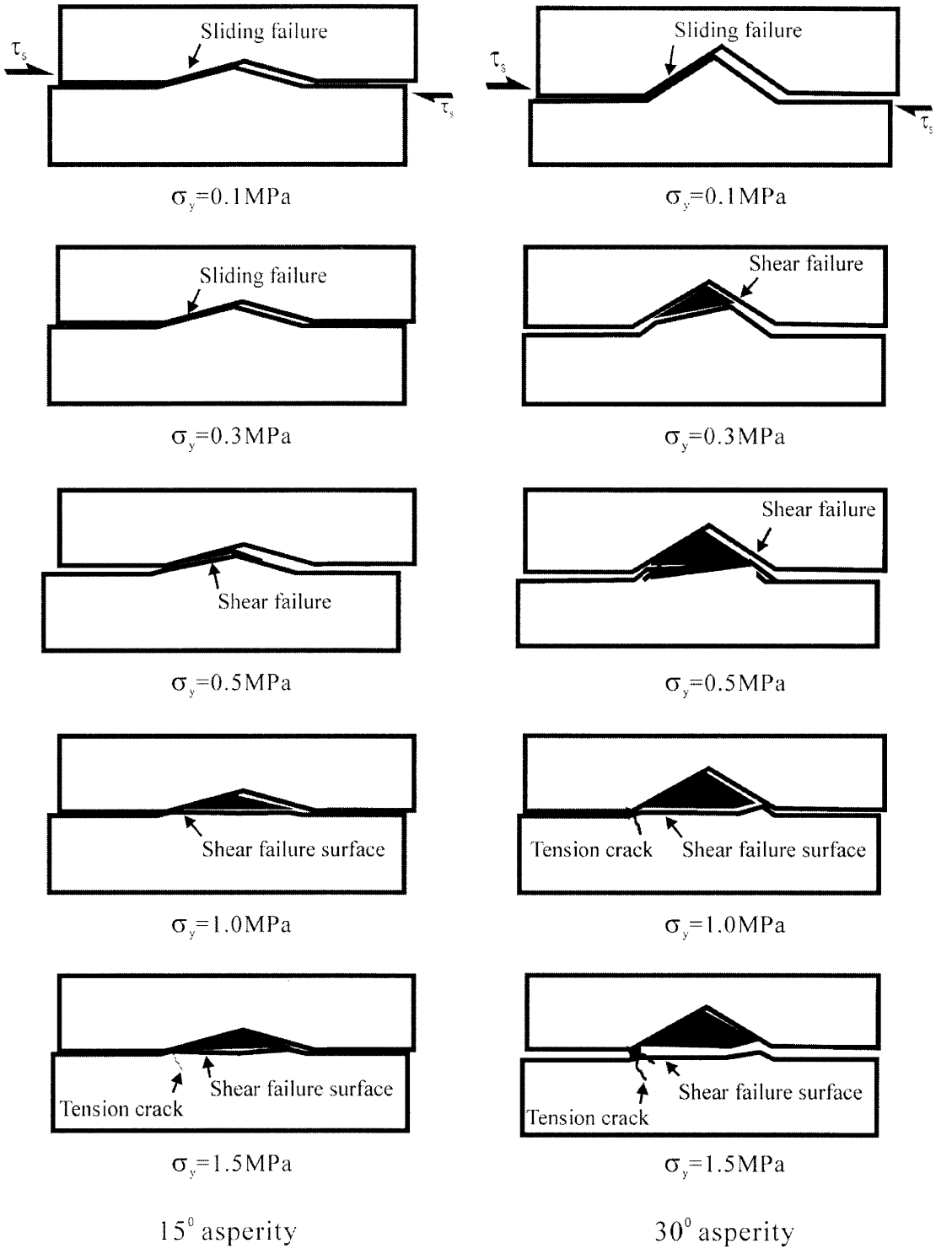

Fig. 9. Failure modes observed in experiments.

Table 1
Observed failure mechanism and orientations of asperity planes after tests

σ_y (MPa)	$\theta = 15°$ α (mechanism)	$\theta = 30°$ α (mechanism)
0.1	15° (sliding)	30° (sliding)
0.3	12° (cut-off)	12.4° (cut-off)
0.5	9.7° (cut-off)	8.5° (cut-off)
1.0	≅0° (cut-off)	≅0° (cut-off)
1.5	≅0° (cut-off)	≅0° (cut-off)

under both $\sigma_y = 1$ and 1.5 MPa, the observed cut-off planes are nearly horizontal. For other magnitudes of applied vertical stresses, the cut-off planes have different angles. A summary of failure mechanisms and the angle of asperity contact planes are given in Table 1.

It is observed that the orientation of cut-off plane is nearly horizontal under a higher vertical stress regardless of the joint topography. Separations were observed at down-slope side of the asperity contacts in both low and high vertical stresses. Crushing is occasionally found on the tips of asperities.

2.2.2. Shear stress–displacement curve

The shear stress–displacement curve can be characteristically divided into four stages: (1) constant stiffness, (2) pre-peak softening, (3) peak stress, and (4) post-peak softening. The magnitude of shear-induced dilation is measured by the dilation angle defined as:

$$\tan\psi = \frac{\Delta u_{\mathrm{n}}}{\Delta u_{\mathrm{s}}} \tag{1}$$

where Δu_{n} and Δu_{s} are respectively the normal displacement and the shear displacement in the dilation curves. The dilation angle ψ is negative in compression and positive in dilation. Dilation angle is very small before peak stress. At the post-peak range, the angle of dilation increases rapidly and eventually becomes a steady-state constant. The steady-state dilation angles are given in Table 2 for various testing conditions.

The dilation angle, for the case of low vertical stress (0.1 MPa), is equal to the inclination angle of the asperity because sliding of the two matching asperities causes the dilation. However, for the case of higher applied vertical stress (0.3–1.5 MPa), the asperity has been cut-off and the dilation angle is equal to the inclination angle of the cut-off plane of the asperity. It is clear that, the dilation after peak stress in this case is a result of sliding along the cut-off plane. Therefore the magnitude of dilation angle decreases with the applied vertical stress on the specimen, following the same trend as the orientation of cut-off plane. When the applied vertical stress is high (1.0 or 1.5 MPa), the dilation angle is repressed to nearly zero.

Table 2
Post-peak steady-state dilation angles obtained from experimental results

σ_y (MPa)	$\theta = 15°$ dilation angle	$\theta = 30°$ dilation angle
0.1	14.57° (sliding)	30.13° (sliding)
0.3	12.41° (cut-off)	12.40° (cut-off)
0.5	7.1° (cut-off)	8.53° (cut-off)
1.0	Flat (cut-off)	Flat (cut-off)
1.5	Flat (cut-off)	Flat (cut-off)

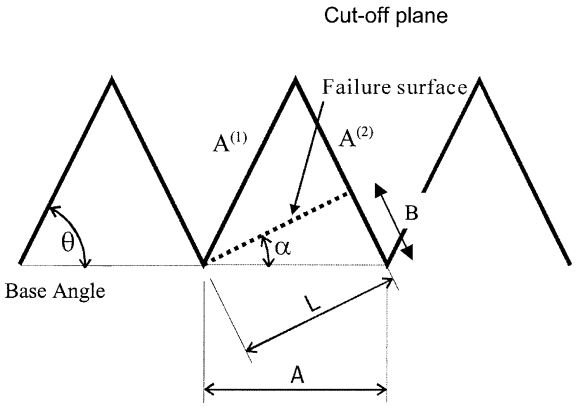

Fig. 10. Schematic plot for triangle-shaped asperities.

3. Model of an asperity

The surface topography of joints consists of triangle-shaped asperities as shown in Fig. 10. Each triangle tooth with two side-faces is termed as an asperity in this paper. Each side-face of the asperity is in contact with a side-face of the matching asperity. Thus two scales of interface are identified: the macroscale interface of joint, and the microscale contact-face of asperity.

In this section, we describe a mathematical model for the behavior of asperity contact-face. At the asperity scale, the contact-face model is phenomenological which will be used in a later section to derive the behavior of joint. For clarity, we define the variables used for the two levels as follows:

(1) Macroscale interface of joint: relative displacements (u_x, u_y), and surface traction (τ_x, τ_y). The subscripts x and y refer to the global coordinate system.
(2) Microscale contact-face of asperities: relative displacements $(u_s^{(c)}, u_n^{(c)})$, and surface traction $(\tau_s^{(c)}, \tau_n^{(c)})$. The subscripts s and n refer to the local coordinate system. The superscript c refers to the contact-face number.

3.1. Asperity contact-face behavior

3.1.1. Normal compression

For the closure of an asperity contact-face due to a compressive stress in the normal direction, we use the following hyperbolic stress–displacement relationship proposed by Bandis et al. [2]:

$$u_n^{(c)} = \frac{\sigma_n^{(c)} V_{\mathrm{m}}^{(c)}}{A^{(c)} k_{\mathrm{ni}}^{(c)} V_{\mathrm{m}}^{(c)} + \sigma_n^{(c)}} \tag{2}$$

where $u_n^{(c)}$ is the normal compressive displacement for the contact-face, $\sigma_n^{(c)}$ is the normal compressive stress, $V_{\mathrm{m}}^{(c)}$ is the maximum closure of the joint, $A^{(c)}$ is the area of asperity contact-face, and $k_{\mathrm{ni}}^{(c)}$ is the initial normal stiffness for the contact-face, which is of the Winkler type with a unit of F/L^3. The contact force $f_n^{(c)}$ is equal to $A^{(c)}\sigma_n^{(c)}$. The superscript c refers to the particular asperity contact-face.

Written in an incremental form, the normal tangential stiffness $k_n^{(c)}$ of the asperity contact-face defined in

$$\Delta f_n^{(c)} = A^{(c)} k_n^{(c)} \Delta u_n^{(c)} \tag{3}$$

can be derived from Eq. (2) as a function of the contact-face displacement $u_n^{(c)}$ given by

$$k_n^{(c)} = \frac{k_{ni}^{(c)} V_m^{(c)}}{V_m^{(c)} - u_n^{(c)}} \tag{4}$$

It can be seen from Eq. (3) that initially when $u_n^{(c)} = 0$, the value of the normal tangential stiffness $k_n^{(c)} = k_{ni}^{(c)}$. When the displacement $u_n^{(c)}$ approaches to the maximum closure of the joint $V_m^{(c)}$ the value of $k_n^{(c)}$ approaches to infinity.

3.1.2. Tangential shear

The shear stiffness $k_s^{(c)}$ of an asperity contact-face is defined in the following expression:

$$\Delta f_s^{(c)} = A^{(c)} k_s^{(c)} \Delta u_s^{(c)} \tag{5}$$

where $\Delta u_s^{(c)}$ is the tangential displacement for the contact-face. The shear stiffness is a function of normal stress of the contact-face, given by

$$k_s^{(c)} = k_{si}^{(c)} \left(\frac{\sigma_n^{(c)}}{P_a} \right)^b \tag{6}$$

where $k_{si}^{(c)}$ is the reference shear stiffness defined as the shear stiffness of the contact-face under the condition that the normal compressive stress $\sigma_n^{(c)}$ is equal to the atmospheric pressure P_a. The exponent b is a constant.

Frictional sliding is governed by the surface frictional angle of the contact-face ϕ_s, given by

$$\frac{\tau_s^{(c)}}{\sigma_n^{(c)}} \leqslant \tan \phi_s$$

When the ratio of the interfacial stress exceeds the frictional resistance, sliding occurs and the tangential shear stiffness $k_s^{(c)} = 0$.

When a contact-face is in compression ($\sigma_n^{(c)} \geqslant 0$), both the normal and shear stiffness can be evaluated as described above. After separation of an asperity contact-face, the compressive stress $\sigma_n^{(c)}$ is null and both the normal and shear stiffness become zero.

3.2. Sliding of asperities

Three types of failure modes for matching asperities are considered: frictional sliding, contact separation, and asperity cut-off. The modes of asperity crush or compressive yielding are found only occasionally on the tips of asperities, thus are neglected for the rock joint modeling in this paper.

Sliding occurs between two matching asperities when the shear force exceeds the frictional resistance on the contact-face. At the event of sliding on the up-slope face together with a separation of the down-slope face, the shear strength of the asperity can be determined by

$$\tau_x = \sigma_y \tan(\phi_s + \xi) \tag{7}$$

where ϕ_s is the surface friction angle of the contact-face, ξ is the up-slope angle. In the case of triangle-shaped asperities as shown in Fig. 10, $\xi = \theta$ before cut-off, and $\xi = \alpha$ after cut-off. Therefore base angle of asperities is an important factor of the shear strength.

3.3. Cut-off of asperities

Cut-offs of asperities are frequently observed, which have significant effects on the strength and therefore is considered in the present model.

3.3.1. Determination of cut-off plane

In order to determine the orientation of cut-off plane, we adopt the *method of limit equilibrium,* which has been traditionally used in soil mechanics for the determination of sliding surface of an unstable slope. The process is to select the most critical cut-off plane from a number of trial planes. The hypothesis is that the most critical plane corresponds to the one that satisfies the cut-off criterion. The procedure is given below.

Consider, for example, an asperity with a base angle θ as shown in Fig. 10. The up-slope area $A^{(1)}$ is equal to the down-slope area $A^{(2)}$ and the base area $A = (A^{(1)} + A^{(2)})\cos\theta$. After the occurrence of a cut-off plane with angle α, surface topography of the asperity is altered. The new up-slope contact-face is and the new down-slope contact-face is B (see Fig. 10), given by

$$L = \frac{A\sin\theta}{\sin(\theta+\alpha)} \tag{8}$$

$$B = \frac{A\sin\alpha}{\sin(\theta+\alpha)} \tag{9}$$

Let $(f_n^{(1)}, f_s^{(1)})$ and $(f_n^{(2)}, f_s^{(2)})$ respectively be the normal and shear forces on the up-slope (left side) and down-slope contact-face (right side) of the triangle-shaped asperity. The forces can be transformed into $(f_x^{(1)}, f_y^{(1)})$ and $(f_x^{(2)}, f_y^{(2)})$, which respectively are the forces on the left side and right side-faces of the triangle-shaped asperity. The total forces for this asperity (f_x, f_y) are

$$f_x = f_x^{(1)} + f_x^{(2)}; \quad f_y = f_y^{(1)} + f_y^{(2)} \tag{10}$$

It is noted that, for the joint with regular asperities, the tractions on the joint surface $\tau_x = f_x/A$ and $\sigma_y = f_y/A$. After cut-off, the down-slope contact-face area has reduced from $A^{(2)}$ to B (see Fig. 10), thus the force on the down-slope face is reduced to $(f_x^{(2)}, f_y^{(2)})B/A^{(2)}$. Based on force equilibrium, the force vector on the cut-off plane, $f_x^{(\alpha 1)}$, $f_y^{(\alpha 2)}$ can be obtained by subtracting the down-slope force from the total force

$$\begin{aligned} f_x^{(\alpha 1)} &= \tau_x A - f_x^{(2)} B/A^{(2)} \\ f_y^{(\alpha 1)} &= \sigma_y A - f_y^{(2)} B/A^{(2)} \end{aligned} \tag{11}$$

The forces $(f_x^{(\alpha 1)}, f_y^{(\alpha 1)})$ can then be transformed to the local coordinate system to obtain the normal and shear forces, $(f_n^{(\alpha 1)}, f_s^{(\alpha 1)})$, on the cut-off plane. Assuming the shear strength of the material against cut-off is determined by a Mohr–Coulomb criterion with cohesion c and frictional angle ϕ the shear force permissible on the cut-off plane, T_s, is given by

$$T_s^{(\alpha 1)} = \tau_s^{(\alpha 1)} L = (c + \sigma_n^{(\alpha 1)} \tan\phi) L \tag{12}$$

When the shear force reaches the permissible limit on a potential cut-off plane, (i.e. $f_s^{(\alpha 1)} = T_s^{(\alpha 1)}$), the cut-off is assumed to occur.

In Eq. (11), the magnitudes of forces on down-slope face, $f_x^{(2)}$ and $f_y^{(2)}$ depend upon the relative contact stiffness of up-slope and down-slope faces. Since the contact stiffness is non-linear and stress-dependent as described in Section 3.1, the magnitudes of $f_x^{(2)}$ and $f_y^{(2)}$ are generally different for each loading case and impossible to determine without detailed analyses. However, if separation of the down-slope face has already occurred, the values of $f_x^{(2)}$ and $f_y^{(2)}$ are zero. In this situation, the critical cut-off plane and the shear force required for cut-off can be solved without detailed analyses. The separation of down-slope face usually occurs under a large shearing deformation, thus the shear strength determined in this condition corresponds to the residual shear strength, which may be different from the peak strength.

For the case of separation of the down-slope face, $f_x^{(2)}$ and $f_y^{(2)}$ are zero in Eq. (11), thus the force vector on the cut-off plane are

$$f_x^{(\alpha 1)} = \tau_x A; \quad f_y^{(\alpha 1)} = \sigma_y A \tag{13}$$

which can be converted to obtain the shear and normal forces, $f_s^{(\alpha 1)}$ and $f_n^{(\alpha 1)}$, in the local coordinate system on the cut-off plane

$$\begin{aligned} f_s^{(\alpha 1)} &= (\tau_x \cos\alpha - \sigma_y \sin\alpha)A \\ f_n^{(\alpha 1)} &= (\tau_x \sin\alpha + \sigma_y \cos\alpha)A \end{aligned} \tag{14}$$

where the vertical stress σ_y is positive in compression.

Using Eqs. (12) and (14), the ratio of the applied shear force over the allowable shear force $F = f_s^{(\alpha 1)}/T_s^{(\alpha 1)}$ on the cut-off plane is

$$F = \frac{(-\tau_x \cos\alpha - \sigma_y \sin\alpha)A}{\tau_s^{(\alpha 1)} L} \tag{15}$$

Substituting the ratio of A/L in Eq. (8), the following equation can be obtained:

$$F = \frac{(-\tau_x \cos\alpha - \sigma_y \sin\alpha)}{\tau_s^{(\alpha 1)}} \frac{\sin(\theta+\alpha)}{\sin\theta} \tag{16}$$

If the value of shear strength is expressed in the form of Mohr–Coulomb criterion, $\tau_s^{(\alpha 1)} = c + \sigma_n^{(\alpha 1)} \tan\phi$, note that $\sigma_n^{(\alpha 1)} = f_n^{(\alpha 1)}/L$, then

$$F = \frac{\dfrac{\tau_x}{c}\cos\alpha - \dfrac{\sigma_y}{c}\sin\alpha}{\dfrac{\sin\theta}{\sin(\theta+\alpha)} + \left(\dfrac{\tau_x}{c}\sin\alpha - \dfrac{\sigma_y}{c}\cos\alpha\right)\tan\phi} \tag{17}$$

As an example, we consider a rock joint with regular asperities similar to that in Fig. 10 with base angle $\theta = 30°$ and friction angle $\phi = 10°$. The rock joint is under a constant vertical stress $\sigma_y = 0.2c$ and an increased shear stress τ_x. Assuming the trial cut-off angle is $\alpha = 8°$, the computed value of F increases with τ_x/c in Eq. (18). When the shear stress ratio $\tau_x = 0.914c$, $F = 1$ and the cut-off occurs. If we repeat the same process for several trials of cut-off angle α, the results are shown in Fig. 11. Among all trial cut-off angles, the minimum value of $\tau_x = 0.854c$ corresponding to $\alpha = 18°$, therefore a $\alpha = 18°$ is the critical cut-off angle.

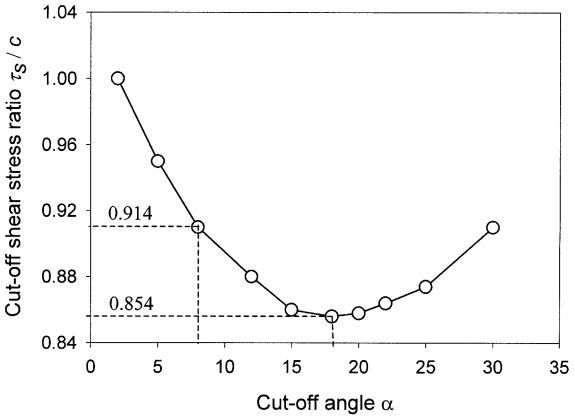

Fig. 11. Trial cut-off angles and correspondent shear stresses.

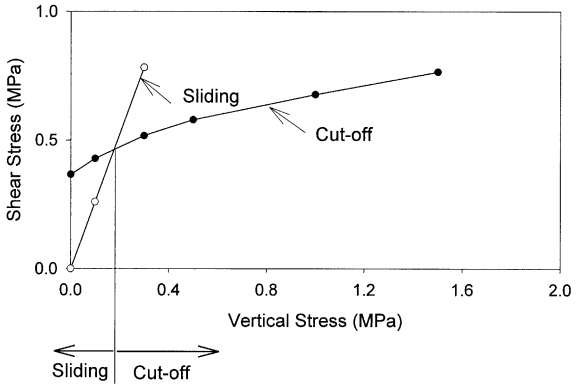

Fig. 12. Shear strength envelope controlled by sliding and cut-off mechanisms.

If the same rock joint is under a higher applied vertical stress $\sigma_y = 1.0c$, the computed minimum value of $\tau_x = 1.15c$ corresponding to the critical cut-off angle $\alpha = 5°$. The cut-off angle and shear strength are clearly influenced by the vertical stress. For this particular example, assuming the value of $c = 0.5$ MPa, the shear strength against cut-off for different applied vertical stress is computed and plotted in Fig. 12. The shear strength against sliding failure determined from Eq. (7) is also plotted in Fig. 12 (with surface frictional angle $\phi_s = 40°$). It can be seen from Fig. 12 that the sliding mechanism controls failure when the vertical stress is less than 0.2 MPa, and the cut-off mechanism controls failure when the vertical stress is greater than 0.2 MPa. It is noted that based on this simple analysis of limit equilibrium, the residual shear strength of a rock joint is influenced significantly by vertical stress and joint topography, which have been recognized from experimental and field investigations [3,21].

4. Joint behavior model

In order to model the deformation behavior before and after peak stress, a more elaborated constitutive model is needed. For this purpose, we adopt a microstructural approach used in granular mechanics [15,22–26]. This approach has the ability to model the overall behavior of a system based on the properties of individual constituent elements. In the present case, we aim to derive the behavior of a rock joint based on the properties of each asperity contact-face.

Let Δu_i be the displacement of the joint where the lowercase subscript, i, represents (x, y) of the global coordinate system. The joint topography is assumed to consist of many asperity contact-faces. An auxiliary local coordinate system (n, s) is defined for each asperity contact-face. The value of $\Delta u_I^{(c)}$ is the displacement at the asperity contact-face c, where the subscript I in upper case represents (n, s) of the auxiliary local coordinate. We adopt the kinematic assumption [14,23,24] that the value $\Delta u_I^{(c)}$ of the contact-face c can be obtained from the displacement Δu_i of the joint, given by

$$\Delta u_I^{(c)} = T_{Ii}^{(c)} \Delta u_i \tag{18}$$

where $T_{Ii}^{(c)}$ is the transformation matrix that transform a vector from the global coordinate system to the local coordinate system of the cth contact-face. The transpose of this transformation matrix $T_{iI}^{(c)}$ is used to transform a vector from the local coordinate system to the global coordinate system. It is noted that T_{iI}^{c} is also the inverse of T_{Ii}^{c}, or

$$T^c_{iI}T^c_{Ij} = \delta_{ij} \tag{19}$$

where δ_{ij} is the Kronecker delta. The forces at the contact-face in the local coordinate system $(\Delta f_s^{(c)}, \Delta f_n^{(c)})$ can be transformed to be in terms of global coordinate $(\Delta f_x^{(c)}, \Delta f_y^{(c)})$ by

$$\Delta f_i^{(c)} = T_{iI}^{(c)} \Delta f_I^{(c)} \tag{20}$$

For an asperity contact-face, the displacement can be related to force by

$$\Delta f_I^{(c)} = A^{(c)} k_{IJ}^{(c)} \Delta u_J^{(c)} \tag{21}$$

where $k_{IJ}^{(c)}$ is the stiffness tensor for the cth contact-face, in a matrix form

$$k_{IJ}^{(c)} = \begin{bmatrix} k_n^{(c)} & 0 \\ 0 & k_s^{(c)} \end{bmatrix} \tag{22}$$

where $k_n^{(c)}$ is the stiffness in normal direction given in Eq. (4), and $k_s^{(c)}$ is the stiffness in tangential direction given in Eq. (6). The force on the rock joint is the summation of forces over all contact-faces, and the traction on the rock joint is given by

$$\Delta\tau_i = \frac{1}{A} \sum_c \Delta f_i^c \tag{23}$$

where A is the total area of the rock joint. Substitute Eqs. (18), (20) and (21) into (23), we obtain the expression of constitutive relationship for the rock joint

$$\Delta\tau_i = D_{ij} \Delta u_j \tag{24}$$

where the stiffness tensor

$$D_{ij} = \frac{1}{A} \sum_c T_{iI}^{(c)} k_{IJ}^{(c)} T_{Jj}^{(c)} A^{(c)} \tag{25}$$

The method described above is valid for a joint surface that consists of irregular asperities. In our case of triangle-shaped asperities as shown in Fig. 10, the surface roughness can be characterized by only two distinctive contact-faces: the up-slope face and the down-slope face. Therefore the total number of contact-face to be considered is two.

Eq. (24) can be written in matrix form, given by

$$\begin{Bmatrix} \Delta\tau_x \\ \Delta\sigma_y \end{Bmatrix} = \begin{bmatrix} D_{xx} & D_{xy} \\ D_{yx} & D_{yy} \end{bmatrix} \begin{Bmatrix} \Delta u_x \\ \Delta u_y \end{Bmatrix} \tag{26}$$

For the rock joint test, two stages of loading are applied. The first stage is the application of vertical stress ($\Delta\tau_x = 0$); the second stage is shearing of joint under the constant vertical stress ($\Delta\sigma_y = 0$). The loads are applied incrementally. At each increment, the stiffness tensors D_{ij} are computed based on the asperity configuration and the stiffness of each contact-face. The asperity configuration is changed after cut-off; and the contact stiffness is dependent on many factors, such as the magnitude of surface tractions, the failure state of the contact-face, e.g. sliding, separation or asperity cut-off. Thus the model is highly non-linear, and an iterative procedure is required. In a load step, the stiffness of each contact-face is initially updated based on the condition before the load. Then, with the computed new condition, the stiffness is re-updated and used to recalculate the same load increment. The iterative process is carried out until the convergence is obtained before the application of the next load increment.

5. Model performance

5.1. Parameters of asperity contact-face

In the analyses of joint behavior, the following six parameters are used:

(1) Compressive behavior of an asperity contact-face: $V_{\max} = 0.8$ mm and $k_{ni} = 1.4$ MPa/mm, determined from the experiments of normal compression tests on joint with 0° asperities (see Fig. 4) and Eq. (4).
(2) Shear behavior of an asperity contact-face: $\phi_s = 39°$, $k_{si} = 0.8$ MPa/mm, $b = 0.45$, determined from the experiments of direct shear tests on joint with 0° asperities (see Fig. 3) and Eq. (6).
(3) Cut-off shear strength: Mohr–Coulomb criterion does not fit the shear strength of the material. The shear strength determined from triaxial tests on rock mass (see Fig. 2) is used in the analysis, given by

$$\tau_s = 0.42 + 0.1246\sigma_n + 0.269\sigma_n^2 + 0.0047\sigma_n^3 \text{ (MPa)}.$$

5.2. Comparisons and discussion

5.2.1. Deformation mechanism

Using the six parameters given above, predictions are made for rock joint specimens under direct shear tests. In a direct shear test, there are two loading stages: (1) initially a vertical compression stress σ_y, and (2) a shear movement u_x. The prediction shows that, due to the vertical load in stage 1, the shear stresses act downward and are equal on both sides of an asperity. In stage 2, due to the shear movement, the shear stress decreases at the up-slope side while increases at the down-slope side. As the shear movement continues, the following events will occur:

(1) slide of the down-slope side,
(2) separation of the down-slope side,
(3) slide of the up-slope side, or cut-off of the asperity.

Among the events, slide of the down-slope side occurs first. Due to the sliding, the overall shear stiffness of rock joint decreases and the shear-induced vertical displacement is downward (i.e., dilation is negative). Separation of the down-slope side usually occurs next. At this point, the overall shear stiffness of rock joint further decreases and the shear-induced vertical displacement starts to reverse its tendency from downward to upward (i.e., dilation is positive).

The next event is either 'slide of the up-slope side' or 'shear cut-off of the asperity'. If 'separation of the down-slope side' has not occurred yet, it will take place concurrently or shortly after. This is the last event in the test. Between sliding and cut-off, which of the two occurs first depends on factors such as the magnitude of vertical stress applied to the rock joint specimen, the material strength, and the surface topography of joint. As a result of the final event, the overall shear stiffness is completely lost and the specimen is in the post-peak softening stage. At the same time, the shear-induced vertical movement continues to be upward (positive dilation). The dilation angle is either same as the up-slope angle or the angle of cut-off plane.

5.2.2. Cut-off plane orientation

The predicted failure modes are in good agreement with the observed failure modes from experiments as shown in Table 3. The predicted cut-off plane orientation is a function of applied vertical stress. For $\sigma_y = 1$ and 1.5 MPa, the predicted shear cut-off planes are nearly horizontal, which are same as what observed in

Table 3
Predicted and measured orientations of asperity planes after tests

σ_y (MPa)	Predicted/measured α (for $\theta = 15°$)	Predicted/measured α (for $\theta = 30°$)
0.1	15°/15° (sliding)	30°/30° (sliding)
0.3	13.5°/12° (cut-off)	14.3°/12.4° (cut-off)
0.5	11.3°/9.7° (cut-off)	8.3°/8.5° (cut-off)
1.0	Flat/≈0° (cut-off)	Flat/≈0° (cut-off)
1.5	Flat/≈0° (cut-off)	Flat/≈0° (cut-off)

experiments. For other applied vertical stresses, the comparisons between the predicted and measured cut-off planes are given in Table 3.

In general, under a higher applied vertical stress, the cut-off plane tends to be more close to horizontal. The comparisons show good agreement between predicted and measured cut-off plane orientations.

5.2.3. Stress–displacement curves

Using the present model, the predicted stress–displacement curves are compared with experimental results for three conditions $\theta = 0°$, 15° and 30°. The comparisons of predicted and measured curves are summarized in Figs. 13–17. Fig. 13 shows the shear stress–displacement curves for joint with 0° asperities. It is noted that for the case of $\theta = 0°$ the shear stiffness determined from Eq. (5) is constant, independent of shear stress. Using a surface frictional angle $\phi_s = 39°$, the stress–displacement curves fit reasonably well the frictional strength. The only failure mode of the joint is frictional sliding. Before sliding, the joint behave elastically without any change of normal stress at contact-face, thus the curves exhibit bilinear shape.

Fig. 14 shows the shear stress–displacement curves for specimens with 15° asperities. The predicted curves for 15° asperities show non-linear rather than bilinear characteristics. During the loading process,

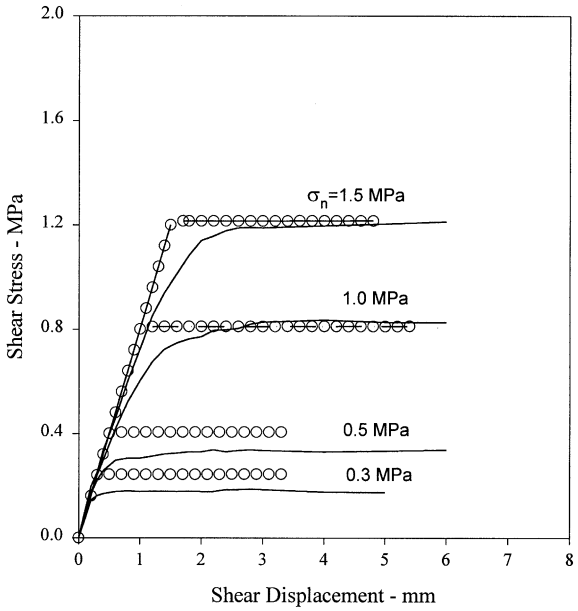

Fig. 13. Comparison of predicted and measured shear stress–displacement curves for joint with 0° asperities.

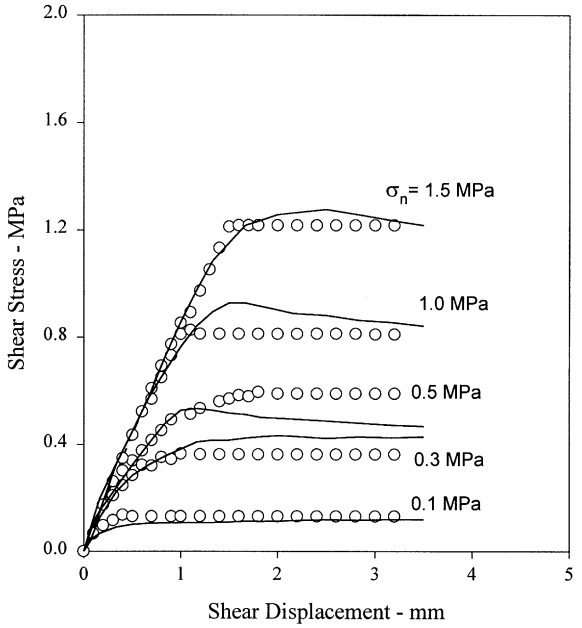

Fig. 14. Comparison of predicted and measured shear stress–displacement curves for joint with 15° asperities.

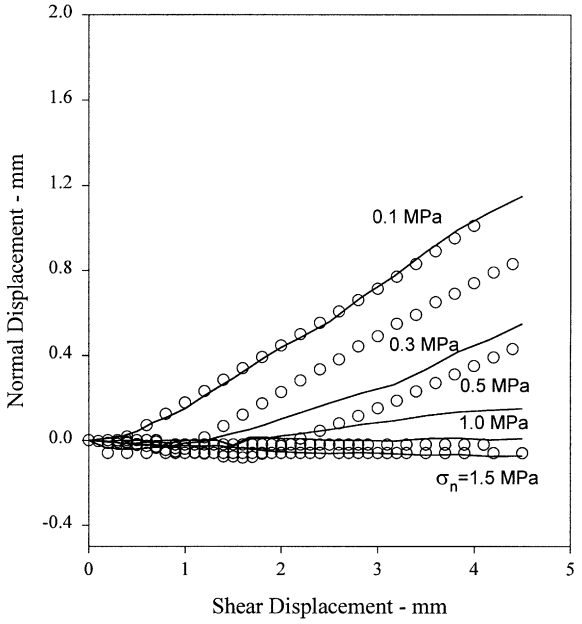

Fig. 15. Comparison of predicted and measured shear dilation curves for joint with 15° asperities.

the specimen has experienced down-slope sliding, down-slope separation, and cut-off of the asperities. At each event, the specimen has a sudden reduction in stiffness. Furthermore, during the loading process, the

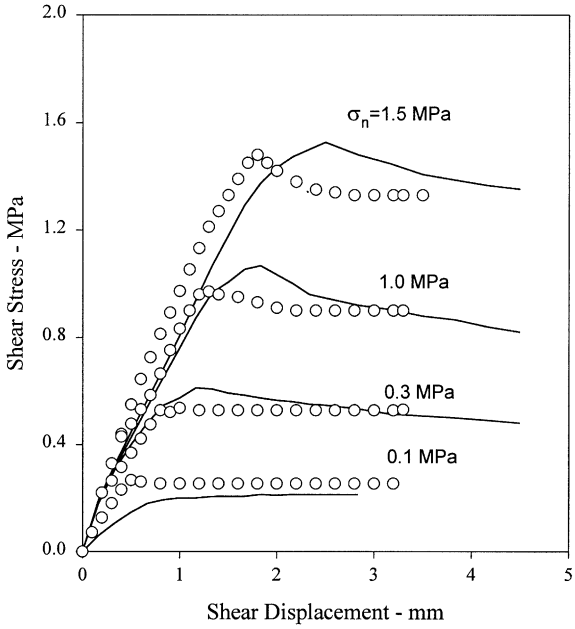

Fig. 16. Comparison of predicted and measured shear stress–displacement curves for joint with 30° asperities.

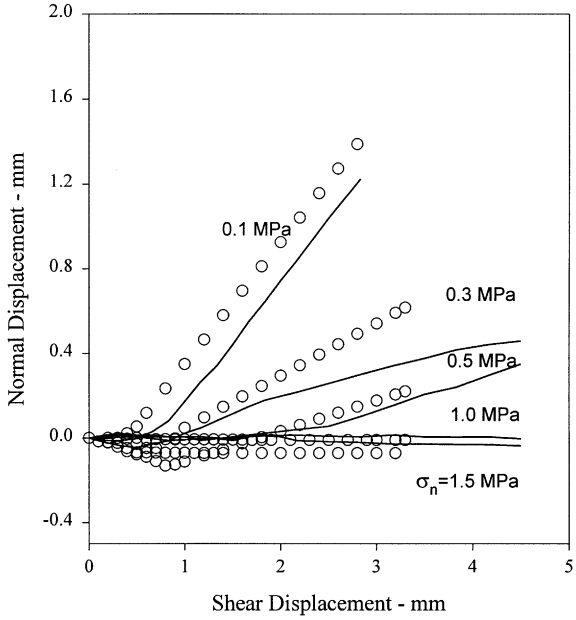

Fig. 17. Comparison of predicted and measured shear dilation curves for joint with 30° asperities.

stiffness of specimen is under a continuous change due to its non-linear dependency with normal stress at contact-faces. Therefore, the predicted curves are rather smooth.

Fig. 15 shows the shear dilation curves for specimens with 15° asperities. Fig. 16 shows the shear stress–displacement curves and Fig. 17 shows the shear dilation curves for specimens with 30° asperities. The overall comparison is reasonable between the predicted and measured results.

5.2.4. Dilation angle

The predicted dilation angle is compared with the measured values in Table 4.

5.2.5. Shear strength

Since the predicted failure modes are in good agreement with that observed from experiments, it is expected that the model give good predictions on shear strength of rock joints. The predicted peak strengths versus vertical stress for the two asperity configurations are plotted in Fig. 18, which verifies the good agreement between the predicted and measured results. Although the peak strength for the rock joint specimens is somewhat different from the residual strength, the method described in Section 3.3 offers a simple and conservative way to estimate shear strength of rock joint.

Table 4
Predicted and measured steady-state dilation angle

σ_y (MPa)	Predicted/measured ($\theta = 15°$)	Predicted/measured ($\theta = 30°$)
0.1	16.69°/14.57°	30.11°/30.13°
0.3	13.49°/12.41°	14.30°/12.40°
0.5	11.31°/7.1°	8.25°/8.53°
1.0	Flat/≈0°	Flat/≈0°
1.5	Flat/≈0°	Flat/≈0°

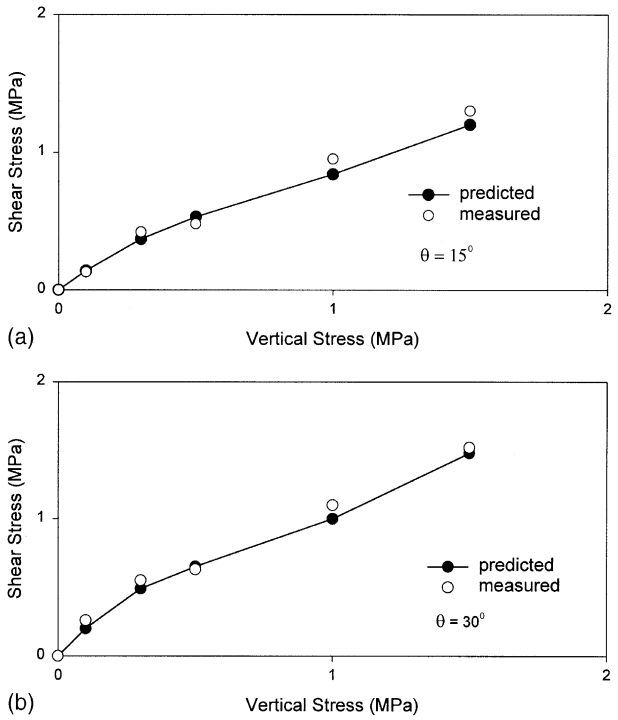

Fig. 18. Comparison of predicted and measured shear strength.

6. Summary and conclusion

A micromechanics model is developed for the stress–displacement behavior of a rock joint which has triangle-shaped asperities on the joint surface. The model explicitly accounts for the influence of asperity shape on the deformation and strength of rock joints. Three mechanisms are considered: sliding of contact-face, separation of contact-face, and cut-off of an asperity, which are essential to be included in order to model the salient features of joint behavior. The agreement between the predicted and measured experimental results shows that the microstructural approach has advantages in simulating the complex behavior. The future work is to extend the present constitutive model to natural rock joints with irregular rough surfaces, which can be used in conjunction with mechanistic models for highly fractured rock masses.

References

[1] Bandis SC, Lumsden AC, Barton NR. Experimental studies of scale effects on the shear behavior of rock joints. Int J Rock Mech Sci Geomech Abstr 1981;20(6):249–68.
[2] Bandis SC, Lumsden AC, Barton NR. Fundamental of rock joint deformation. Int J Rock Mech Sci Geomech Abstr 1983;20(6):249–68.
[3] Barton NR, Bandis SC, Bakhtar K. Strength deformation and conductivity coupling of rock joints. Int J Rock Mech Sci Geomech Abstr 1985;22(3):121–41.
[4] Greenwood JA, Williamson JBP. Contact of nominally flat surfaces. Proc R Soc London 1966;A295:300–19.
[5] Swan G. Determination of stiffness and other joint properties from roughness measurements. Rock Mech Rock Eng 1983;16:19–38.
[6] Brown SR, Scholz CH. Closure of rock joints. J Geophys Res 1986;91:4938–48.
[7] McCool JI. Comparison of models for the contact of rough surfaces. Wear 1986;107:37–60.
[8] Chang WR, Etsion I, Bogy DR. An elastic–plastic model for the contact of rough surfaces. J Tribol, ASME 1987;109:257–63.
[9] Yamada K, Takeda N, Kagami J, Naoi T. Mechanisms of elastic contact and friction between rough surfaces. Wear 1978;48:15–34.
[10] Swan G, Zongqi S. Prediction of shear behavior of joints using profiles. Rock Mech Rock Eng 1985;16:19–38.
[11] Yoshioka N, Scholz CH. Elastic properties of contacting surfaces under normal and shear loads—2. Comparison of theory with experiment. J Geophys Res 1989;94:17691–700.
[12] Boitnott GN, Biegel RL, Scholz CH, Yoshioka N, Wang W. Micromechanics of rock friction—2. Quantitative modeling of initial friction with contact theory. J Geophys Res 1992;97:8965–78.
[13] Ford IJ. Roughness effect on friction for multi-asperity contact between surfaces. J Phys D: Appl Phys 1993;26:2219–25.
[14] Misra A. Mechanical model for contact between rough surfaces. J Eng Mech, ASCE 1997;123(5):475–84.
[15] Misra A. Micromechanical model for anisotropic rock joints. J Geophys Res 1999;104(B10):23175–87.
[16] Yoshioka N. A review of the micromechanical approach to the physics of contacting surfaces. Tectonophysics 1997;277:29–40.
[17] Deere DU, Merritt AH, Coon R. Engineering classification of in-situ rock. Int J Rock Mech Mining Sci 1973;4(5):177.
[18] Chao CY. A study on hydro-mechanical coupling behavior for rock joint. PhD Thesis. National Taiwan University, Taipei, Taiwan, 1999.
[19] Handanyan JM. The role of tension in failure of jointed rock. In: Proceedings of International Symposium on Rock Joints, Leon, Norway, 1990. p. 195–202.
[20] Pereira JP, de Freitas MN. Mechanism of shear failure in artificial fractures of sandstone and their implication for models of hydromechanical coupling. Rock Mech Rock Eng 1993;26(3):195–214.
[21] Barton NR, Choubey V. The shear strength of rock joints in theory and practice. Rock Mech 1977;10(1–2):1–54.
[22] Chang CS, Huang TH. A constitutive model for jointed rock masses. J Chin Inst Eng 1989;11(1):25–34.
[23] Chang CS, Chang Y, Kabir M. Micromechanics modelling for the stress–strain behavior of granular soil—I: Theory. J Geotech Eng, ASCE 1992;118(12):1959–74.
[24] Chang CS, Kabir M, Chang Y. Micromechanics modelling for the stress–strain behavior of granular soil—II: Evaluation. J Geotech Eng, ASCE 1992;118(12):1975–94.
[25] Huang TH, Chang CS, Yang ZY. Elastic moduli for fracture rock mass. Rock Mech Rock Eng 1995;28(3):135–44.
[26] Yoshioka N, Scholz CH. Elastic properties of contacting surfaces under normal and shear loads 1. Theory. J Geophys Res 1989;94:17681–90.